ADVANCED OPTICAL MATERIALS
www.advopticalmat.de

Plasmonic Photochemistry as a Tool to Prepare Metallic Nanopores with Controlled Diameter for Optimized Detection of Single Entities

German Lanzavecchia, Joel Kuttruff, Andrea Doricchi, Ali Douaki, Krishnadas Kumaranchira Ramankutty, Isabel García, Lyuye Lin, Alba Viejo Rodríguez, Thomas Wågberg, Roman Krahne, Nicolò Maccaferri, and Denis Garoli**

Plasmonic solid-state nanopores with tunable hole diameters can be prepared via a photocatalytic effect resulting from the enhanced electromagnetic (EM) field inside a metallic ring on top of a dielectric nanotube. Under white light illumination, the plasmon-enhanced EM-field induces a site-selective metal nucleation and growth within the ring. This approach is used to prepare Au and bimetallic Au–Ag nano-rings and demonstrate the reduction of the initial inner diameter of the nanopore down to 4 nm. The tunability of the nanopore diameter can be used to enable optimized detection of single entities with different sizes. As a proof-of-concept, single object detection of double stranded DNA (dsDNA) and Au nanoparticles (AuNPs) with a diameter down to 15 nm is performed. Numerical simulations provide insights into the EM-field distribution and confinement, showing that a field intensity enhancement of up to 10^4 can be achieved inside the nanopores. This localized EM-field can be used to perform enhanced optical measurements and generate local heating, thereby modifying the properties of the nanopore. Such a flexible approach also represents a valuable tool to investigate plasmon-driven photochemical reactions, and it can represent an important step toward the realization of new plasmonic devices.

1. Introduction

Nanopore technology is the core of third-generation sequencing, and solid-state nanopores are now one of the main topics in single-molecule sensing. In order to make solid-state nanopores a valid alternative to the more commonly used biological nanopores, different nanofabrication methods and materials have been developed so far.[1–6] Electrical measurements are the main approach for single-molecule detection and sequencing by means of nanopores. Unfortunately, electrical readout is complex to be applied to parallel detection from multiple nanopores, while readout schemes that rely on optical spectroscopy can make it possible with high efficiency.[7–11] In this context, plasmonic nanopores represent a unique tool to reduce the shot noise from the optical signal of small objects and molecules via the local enhancement of the electromagnetic (EM)

G. Lanzavecchia, A. Doricchi, A. Douaki, L. Lin, R. Krahne, D. Garoli
Optoelectronics Group
Istituto Italiano di Tecnologia
via Morego 30, Genova I-16163, Italy
E-mail: denis.garoli@iit.it

G. Lanzavecchia
Dipartimento di Fisica
Univesità di Genova
Via Dodecaneso 33, Genova 16146, Italy

J. Kuttruff
Department of Physics
Universität Konstanz
Universitätsstraße 10, 78464 Konstanz, Germany

A. Doricchi
Dipartimento di Chimica
Univesità di Genova
Via Dodecaneso 31, Genova 16146, Italy

K. Kumaranchira Ramankutty, I. García
CIC biomaGUNE
Basque Research and Technology Alliance (BRTA)
Donostia-San Sebastián 20014, Spain

I. García
Biomedical Research Networking Center in Bioengineering, Biomaterials, and Nanomedicine (CIBER-BBN)
Donostia-San Sebastián 20014, Spain

A. Viejo Rodríguez, N. Maccaferri
Department of Physics and Materials Science
University of Luxembourg
106A Avenue de la Faïencerie, Luxembourg L-1511, Luxembourg
E-mail: nicolo.maccaferri@umu.se

T. Wågberg, N. Maccaferri
Department of Physics
Umeå University
Linnaeus väg 24, Umeå 901 87, Sweden

N. Maccaferri
Umeå Centre for Microbial Research
Umeå University
Umeå SE-90187, Sweden

The ORCID identification number(s) for the author(s) of this article can be found under https://doi.org/10.1002/adom.202300786

DOI: 10.1002/adom.202300786

field of the incident light used to detect the signal of these small entities, such as DNA and even single proteins. The EM-field enhancement can be confined inside the diameter of the nanopore, down to the nm^3 volume, and engineered by leveraging on the size, shape and material composition of the nanostructure.[8] In the past 10 years, we have witnessed a growing interest in developing different types of plasmonic nanopores for single nanoparticle or molecule detection and sequencing, and more recently to achieve single protein resolution.[12–28] In most cases, the fabrication of sub-10 nm pores requires complex multi-step processes, including Transmission Electron Microscopy (TEM)-assisted sculpturing of the membrane where the plasmonic nanostructures are prepared by using other techniques, such as focus-ion-beam or electron-beam lithography (FIB or EBL, respectively).[29] Intriguing alternative strategies for plasmonic nanopore fabrication have been reported: for instance, optical control of the dielectric breakdown of the membrane has been demonstrated by several groups,[18,30–32] and more recently the use of laser-driven fabrication of nanometric pores received significant interest within the community.[33–35] Nowadays, these approaches enable to prepare solid-state nanopores on dielectric or semiconductor membranes with good reproducibility, however, mainly on the single nanopore level. Therefore, the preparation of nanopore arrays for parallel single molecule detection with controlled diameter, or the fabrication of nanopores in plasmonic materials, such as noble metals, is still challenging.[8,36,37] Methods for metallic nanopore fabrication can be achieved by pore shrinking by means of metal growth or evaporation.[3] Although this procedure is scalable to a large number of pores, it suffers from two major drawbacks: i) it increases the thickness of the pore significantly, thus reducing the spatial confinement of the EM-field; ii) it is applied to the whole substrate. Therefore, metal deposition processes that can be spatially controlled on the nanoscale (without the use of lithographic processes) are highly desirable and represent a key advancement for plasmonic nanopore technology. A possible way to achieve this is by plasmonic photochemistry,[38–40] which refers to a synergistic combination of plasmonics and chemistry on the nanoscale to control metal nucleation and growth.[40,41–46] Here, we demonstrate a scheme to prepare single (3D) plasmonic nanopores, as well as nanopores array with arbitrary configurations. Our design comprises a metallic ring on top of a dielectric tube as illustrated in **Figure 1**. The EM-field enhancement inside the ring is used to trigger localized metal nucleation and growth, thus reducing the diameter of the hole. We demonstrate that the process can be applied to different metals (for instance Au and Ag), albeit with different efficiencies. In particular, for Ag growth, the photocatalytic metal deposition tends to be slow (in the order of 1 nm min^{-1}), enabling a controlled reduction of the nanopore hole diameter down to 4 nm. Fine control of the size of the prepared nanopores is particularly important if the same platform concept is applied for the detection of different single entities. As a proof of concept, we demonstrate that the nanopores fabricated with this photocatalytic approach can be used to detect, via electrical measurements, both large objects, such as nanoparticles with sizes of a few tens of nanometres, and small molecules such as double-stranded DNA (with diameter in the order of 1 nm). Finally, the EM-field enhancement enables biomolecule detection by Surface Enhanced Raman Scattering (SERS), thus enabling also parallel optical read-out.

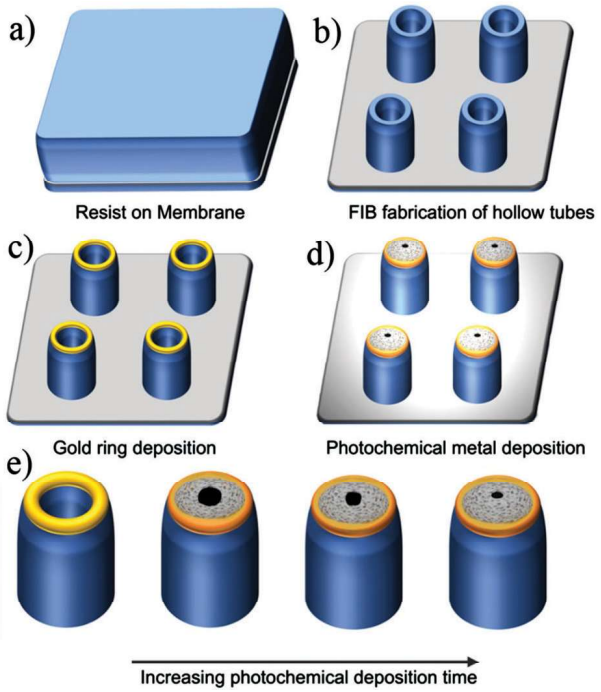

Figure 1. Illustration of the fabrication procedures. a–c) A gold ring is prepared on top of a dielectric nanotube in order to produce a confined and enhanced EM-field.[47] d) This structure is used in combination with photochemistry for sub-5 nm nanopore fabrication. The structure, which consists of a hollow dielectric 3D nanotube with a 30 nm thick gold ring covering its top surface (see Experimental Section for more details), is illuminated with white light and immersed in a metallic salt solution. The EM-field is mainly confined in the inner part of the ring, with a maximum field intensity of up to 10^3.[47] A small EM-field enhancement is also present at the outer part of the Au ring with a maximum intensity of up to 10^2. Considering plasmon-driven metallic nucleation,[40,42] it is reasonable to expect that such field confinement and enhancement can drive the local nucleation of metallic nanoparticles during a photochemical reaction. Hence, under illumination (d) a significantly increased growth rate of metals can be expected due to the field enhancement, mostly in the inner part of the gold ring, and to a smaller extent on the external edges. e) By increasing the photochemical reaction time it is possible to obtain pores with a diameter down to 4 nm.

2. Results and Discussion

Figure 1 illustrates the steps of fabrication of metallic nanopores with nm-precision in an ordered array or in arbitrary arrangement, by exploiting plasmonic photochemistry together with the ability of a metallic ring to confine and enhance the EM-field in its inner part to enable nucleation and growth of an additional metal layer.

In order to excite the EM-field and to enable the photochemical reaction, the samples are illuminated with white light using an optical microscope, similar to the experiment reported by Ai et al.[40] who applied the plasmonic photochemical growth to planar nanoholes on a glass substrate, so decorating the hole with Ag NPs, reaching minimal aperture diameters of 30 nm. Here, we

use a hollow nanopore configuration with a 3D geometry reaching an aperture diameter of a few nm. In order to perform a direct comparison between the 3D design and the planar configuration where the pores are prepared on a thin membrane, both designs will be discussed.

2.1. Nanopore Fabrication

First, we verified the photochemical reaction in a planar configuration considering arrays of gold nanopores (with inner diameters of 70 nm) with a different pitch between 400 and 850 nm. In this case, the EM-field in the inner part of the pores mainly depends on the pitch (periodicity) of the array as verified by finite element method (FEM) simulations (see Experimental Section). We tested the planar configuration using monochromatic light excitation (638 nm) for arrays with varying periodicity. The most effective pitch for EM-field confinement in the pore (see Note S1, Figure S1, Supporting Information) is close to 600 nm. Arrays of nanopores with a pitch varying between 400 and 800 nm were fabricated (see Experimental Section) and used as a platform to grow Ag via the photochemical reaction. As can be observed in Figure S2 and Note S2 (Supporting Information), and in agreement with the FEM simulations, the most efficient plasmonic-driven Ag growth is obtained for a pitch of 600 nm. However, the approach using this configuration did not result in reproducible Ag rings and did not provide the required control in size and uniformity over the array. This is partially in disagreement with the results obtained in ref. [40], and is likely attributed to substrate effects, since in our case the Ag growth was performed on nanoholes in a thin membrane. The absence of a substrate probably limits the efficiency of nucleation because of a smaller EM-field confinement and a different interaction between the metal salts and the substrate. However, the fabrication results obtained for the planar configuration are instructive and informative toward the design and expectations regarding the 3D nanotube-Au-ring geometry.

Then, we experimentally explored the fabrication of the proposed plasmonic nanopores on 3D nanostructures prepared on Si_3N_4 membranes. We first fabricated the metallic rings on top of dielectric tubes (Figure 1a–c). This fabrication relies on a well-established method first reported by De Angelis et al.[48] that was further developed during the last decade.[47,49,50] The principle relies on the FIB-generated secondary-electron lithography in optical resist and allows the preparation of high aspect ratio structures with any 3D profile. The nanotube is prepared on a transparent substrate (100 nm thick Si_3N_4 membrane) with a skeleton made of S1813 optical resist exposed with a secondary electron during its milling to create the desired shape. The versatility of the process allows to prepare 3D structures with high reproducibility, since the size (inner and outer diameters) depends only on the current used during the FIB milling (see Experimental Section). **Figure 2**a,d reports examples of gold rings prepared on top of dielectric tubes with different initial sizes (additional examples of array fabrication can be observed in Note S3, Supporting Information). The ionic current used for the FIB fabrication ranges from 24 to 230 pA, and the obtained rings have external diameters between 200 and 550 nm, resulting in different resonant configurations for the confined field in the inner part of the rings.[47] It is expected that the efficiency in metal ion nucleation during the plasmonic photochemical process depends on the dimension of the gold ring, since the process is related to the EM-field intensity distribution. We compared the process using Au salts ($AuBr_3$ and $HAuCl_4$) and Ag salts ($AgNO_3$). In both cases, the structures have been illuminated with white light (Xe lamp, 50 W, focusing the light on the sample by means of a 20× (0.95 NA) objective). During the exposure, the sample was immersed in the solutions for variable intervals of time between 10 and 50 min, in order to investigate the growth rate. The growth reaction was then stopped by transferring the sample into isopropyl alcohol and finally drying under N_2 flow.

Both Au and Ag nucleation and growth lead to hole shrinking. Scanning electron microscopy (SEM) and Energy Dispersive Spectroscopy (EDS) have been performed to investigate the local deposition morphology and composition (Figure 2). EDS analysis confirmed that the Ag growth is localized on the pillar, with only negligible deposition on the metallic substrate (see Note S4, Supporting Information). No data is reported for Au growth because it was not possible to observe any differences in the EDS maps. Even though the photochemical reaction takes place mainly inside the nanorings, the whole substrate is also coated with Au by the initial deposition. Figure 2i–k reports also an example of the photochemical Ag growth over an array of Au nanorings (see also Note S3, Supporting Information).

We estimated the growth rate by measuring the internal pore diameter with SEM and averaged the measurements over an array of 50 pores. Pore sizes were measured every 10 minutes of reaction under light exposure. The hole shrinking rate observed for silver growth, using 5 mM $AgNO_3$ and Sodium Citrate as a reducing agent,[40] was ≈1 nm min^{-1} as shown in Figure S7 and Note S1 (Supporting Information). It is worth noticing that the field confinement that drives the plasmon-induced metal growth should increase in the inner surface of the nanopore when the pore diameter approaches tiny sizes, thus increasing the growth rate.

We first tested gold deposition via self-reduction of gold from $HAuCl_4$, which led to a slow but rather inhomogeneous process resulting in a poor control of hole shrinking (Note S6, Supporting Information). When replacing the $HAuCl_4$ with $AuBr_3$ salt and Sodium Citrate as a reducing agent, the reaction resulted to be fast with a full blocking of the pores after 15 min reaction time and with significant growth also on the substrate. Similar experiments were conducted with lower concentrations of Au (10% and 1% of the original concentration) resulting in a slower growth rate, but still significant metal deposition on the substrate was observed. At 0.5 mM Au precursor concentration, the pore shrinking rate (measured as described above) was ≈3 nm min^{-1} (Note S7, Supporting Information).

The choice of metallic nanoring on top of a dielectric pillar has an important impact on the spatial distribution of the metal growth. In principle, one could also use a fully Au-covered 3D pillar for the growth, but then the EM-field confinement is extended along the full length of the hollow pillar (at resonance), and not limited to the top part of the pillar as for the metallic nanoring.[47–50] As expected, the seeding (due to plasmon-enhanced photochemical reactions) for fully Au-covered pillars produced metal deposition all over the structure (see Note S8, Supporting Information).

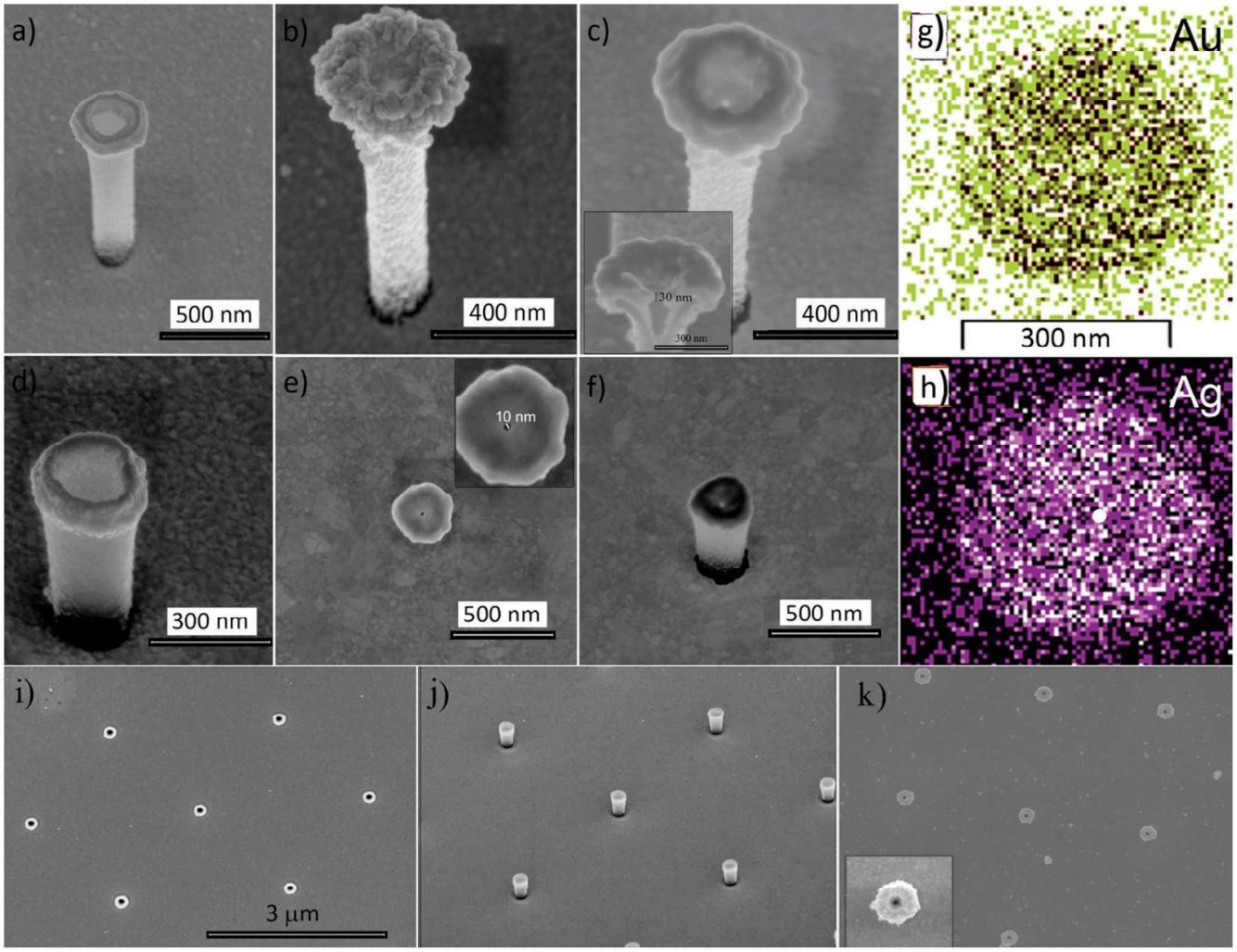

Figure 2. a–f) SEM micrographs of nanopores prepared via plasmonic photochemistry; a,d) examples of an Au ring on top of dielectric pillars prepared at FIB currents of 40 and 80 pA, respectively; b) morphology of the ring after 40 min of photochemical Ag reaction; c–f) examples of the corresponding Ag nanopore morphology (a–d) after thermal annealing (inset c: cross section of the nanopore); g,h) EDS maps of the ring for Au (g) and Ag (h) – the maps are referred to the sample illustrated in panels (e,f); i,j) example of array prepared with a current of 24 pA; k) example of array of nanopores after Ag photochemical growth (after 40 min under light exposure).

The structures obtained and illustrated in Figure 2 and Note S3 (Supporting Information) demonstrate the localized growth of metal obtained with optical excitation. The morphology appears very rough, and therefore with a reduced control on the final shape and thickness of the grown layer. However, the obtained low growth rate enables a fine control on the pore size that is better compared to previously reported metal growth in nanopores, for example, performed via electroless electrochemical depositions.[51–53]

In order to obtain a smooth metallic structure, the samples have been annealed at 200 °C for 10 min under N_2 flux (Figure 2c,e,f; Figure S12, Note S9, Supporting Information). The annealing step is particularly effective in the case of Ag growth, where the large grains obtained after the photochemical reaction are almost completely converted into a smooth metal film after thermal annealing. The most important effect of thermal annealing is that it enabled to obtain inner nanopore diameters smaller than 10 nm in a controlled way. The thermal annealing also modified the shape of the metal ring producing a curvature in the inner part with a final bowl-like shape. To verify that the metal deposition is indeed occurring by a photochemical process, we performed the reaction also without illumination. As illustrated in Figure S13 (Supporting Information), after 30 minutes of reaction in the dark with $AgNO_3$, no Ag deposition was observed inside the Au rings (Note S10, Supporting Information), hence demonstrating the key role of the plasmonic field confinement and enhancement. Finally, as reported in the Experimental Section, the fabrication of the nanopores included a last step of atomic layer deposition of Al_2O_3 (≈1 nm). This is used to passivate the metal layer and avoid potential charge effects.

2.2. Numerical Simulations

We performed FEM simulations to obtain an estimation of the performance of our structures in terms of EM-field confinement

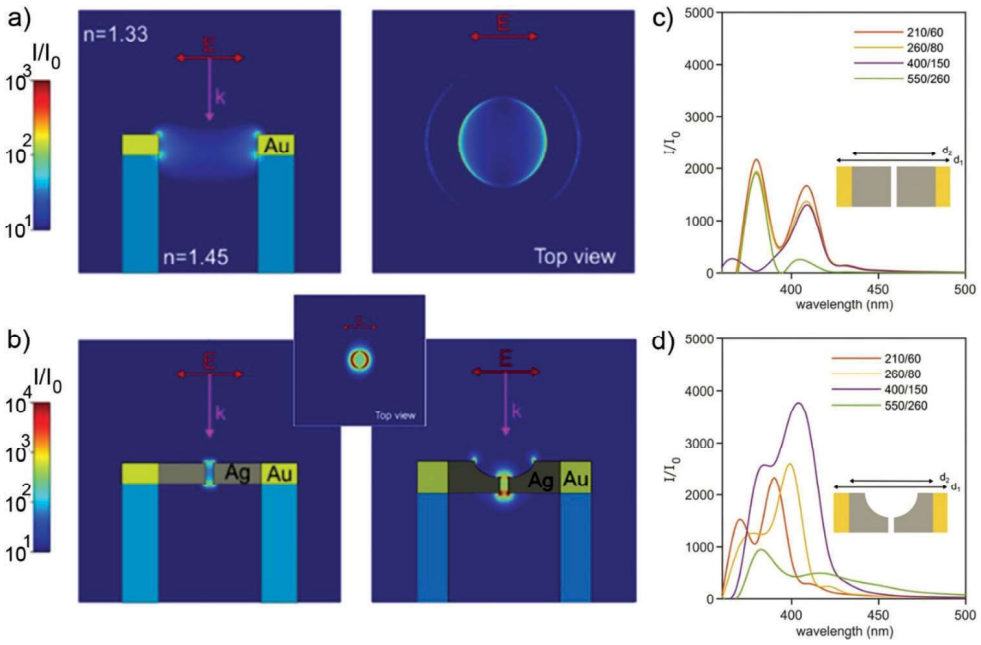

Figure 3. a) Electric field intensity enhancement I/I_0 with logarithmic color scale for the gold ring structure (outer diameter $d_1 = 210$ nm and inner diameter $d_2 = 140$ nm) at resonance condition ($\lambda = 665$ nm). Incident k-vector and polarization are indicated by magenta and red arrows, respectively; b) the bimetallic Ag–Au ring with a pore diameter of 10 nm at resonance ($\lambda = 410$ nm), the left panel shows the planar configuration, right panel the bowl-like structure; c) EM-field intensity enhancement I/I_0 as a function of the wavelength for the planar Au/Ag geometry using different sizes d_1/d_2 as indicated in the inset. The enhancement factor is evaluated as average on the top surface of the nanopore; d) same as in (c) for the bowl-shaped geometry.

and enhancement. In more detail, we used the RF Module in Comsol Multiphysics, taking the geometry of the hollow pillars coated with metal rings into account (**Figure 3**). The top view in Figure 3a shows that the EM-field is mainly confined in the inner part of the ring, with a maximum field intensity of up to 10^3. A small enhancement is also present at the outer part of the ring, where the maximum intensity reaches 10^2. Figure 3b–d illustrates the behaviour of the structure after the inner diameter of the pore was reduced by the Ag deposition (simulations for Au deposition are reported in Note S11, Supporting Information). Figure 3 shows that the reduction of the pore diameter leads to a stronger EM-field enhancement up to a maximum of 10^4 at resonance (410 nm wavelength). Figure 3c shows the calculated intensity enhancement I/I_0 in the nanopores with an ideal geometry, and of the bowl-shaped metal rings (Figure 3d) that are obtained in our fabrication (see Figure 2c,e,f). The bowl-shaped structure obtained with the annealing displays a stronger EM-field enhancement (approximately twice that of the planar structure illustrated). Bowl-shaped nanopores have been recently reported using more complex fabrication procedures, but still demonstrating improved performance in single-molecule translocation and detection.[54] Similar simulations for nanopores with additional Au deposition are reported in Figures S14, S15 and Note S11 (Supporting Information), which reveal a maximum intensity enhancement I/I_0 up to 150 at 610 nm excitation wavelength. The broad response of the Au nanopore in the visible spectral range suggests its potential use in enhanced spectroscopies. This holds also for the Ag-reduced nanopores, although their functionality is optimized at shorter wavelengths.

2.3. Single Entity Detection and Electro-Optical Characterization

To test the performance of our structures in different applications, in particular in single molecule detection, we investigated the nanopores with respect to the following aspects: i) the effect of illumination on the nanopore conductance; ii) the capability of the nanopore, prepared with different pore diameters, to detect single nanoparticles and biomolecules; iii) potential enhanced spectroscopy capabilities for parallel optical readout.

In order to characterize the electrical conductance of the nanopores, we fabricated a single pore on the Si_3N_4 membrane, applying the photochemical reaction with Ag to reduce the hole of the nanopore to a diameter below 10 nm. The conductance was measured by current–voltage (I–V) sweeping and used to evaluate the hole diameter of the pore (**Figure 4**a; Note S12, Supporting Information for details). The samples were placed in a microfluidic chip and immersed in TE buffer (10 mM Tris-HCl containing 1 mM EDTA•Na_2, pH 8). Two AgCl electrodes have been used in combination with a nanopore reader[55] (see Experimental Section for more details). In all cases, the conductance of the nanopore has been measured before and after the photocatalytic metal deposition. We repeated these measurements on different samples and observed that a nanopore with a starting diameter of 60 nm resulted in a reduction by one order of magnitude, down to 4 nm. In the calculation of the pore diameter, it is important to consider the uncertainty in the final pore's thickness due to the fabrication procedure. We evaluated the nanopore thickness by inspection of a cross section of the nanopore obtained by FIB milling (see Figure 2c, inset). Although the method is partially destructive, it enables to estimate a thickness of ≈30 nm after the

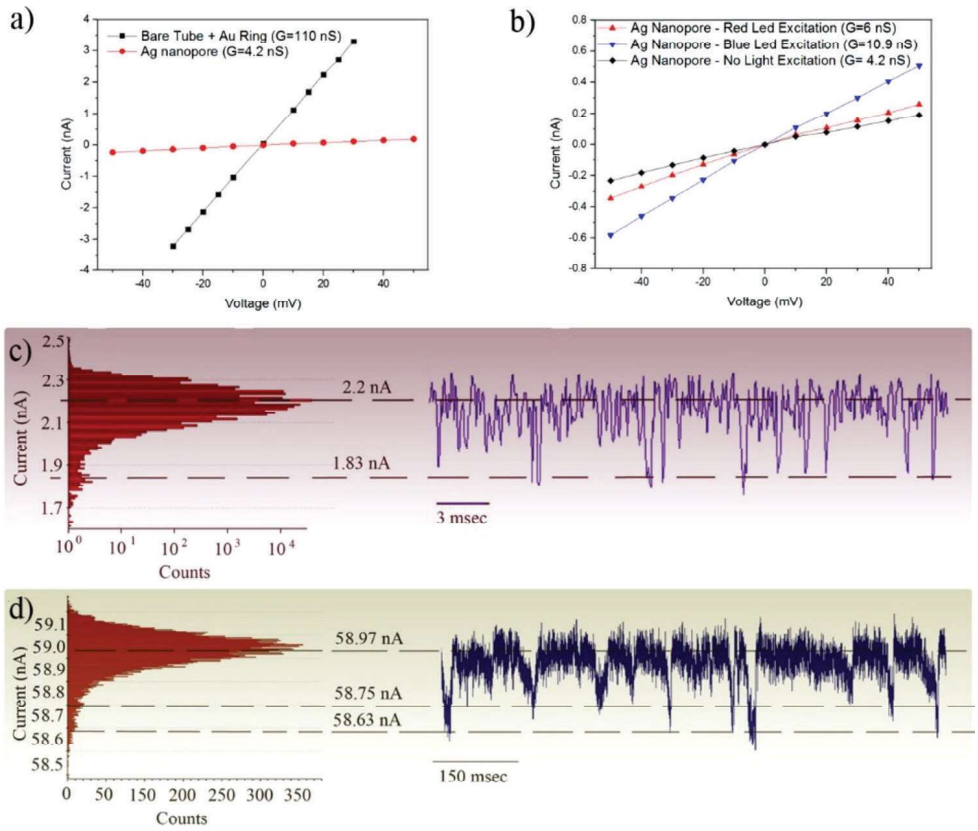

Figure 4. a) *I–V* curves obtained from a single nanopore with an Au ring, and the same nanopore after Ag deposition (after 40 min under white light illumination); b) *I–V* curves of a single Ag–Au nanopore illuminated with different light sources; c) dsDNA translocations in 1 M KCl at $V = 300$ mV. A 20 kHz low-pass Bessel filter is applied to distinguish event characteristics against noise. Translocation event shapes are consistent with single DNA translocation, although no clear discrimination between folded and unfolded states can be observed; d) AuNP (15 and 30 nm) translocations in 1 M KCl at $V = 500$ mV were recorded at 20 kHz bandwidth using the portable nanopore reader from Elements SRL. Few translocation events can be detected per second, where two distinct levels can be associated with 15 and 30-nm particles.

annealing step. This pore thickness correlates to a minimum diameter of 4 nm considering the measured conductance of 4.2 nS (Figure 4a). Worth noticing, the same conductance considering a pore thickness of 150 nm gives a pore diameter of 8.9 nm.

It is important to stress that, although the preparation of a single nanopore with a diameter of a few nm has already been reported in the literature,[9,56–60] the controllable preparation of a metallic (plasmonic) nanopore array with a diameter between tens of nm down to 5 nm is still very challenging.[61] The method proposed here enables a controlled diameter reduction of the nanopore (1 nm min^{-1} with Ag growth) both in single pore configuration and in arrays with arbitrary pores shapes and arrangements. The EM field distribution in a solid-state nanopore has a fundamental role in the translocation process, and controlling the translocation process can enable significant improvements in molecule capturing, spectroscopic investigation,[8,37] and temporal resolution. Obtaining metallic nanopores with plasmonic properties that enable EM field engineering has also the advantage that thermal effects can be explored. To investigate the thermal effects, a simple strategy could be to monitor the nanopore conductance with and without external light stimuli.[17,62,63] Thus, we measured the *I–V* response of the single plasmonic nanopore illuminated with light-emitting diodes (LEDs) at different wavelengths (460 nm (blue) and 650 nm (red), ≈ 2 mW power), respectively. In the Ag-reduced nanopore, we expect to observe a more pronounced plasmonic effect with the blue LED. Our measurements, reported in Figure 4b, demonstrate an increased pore conductance for illumination with blue light (on-resonance) to G = 10.9 nS. This is probably due to the EM-field enhancement produced by the Ag ring, which results in local plasmonic heating of the pore. Measurements off-resonance and without illumination lead to lower conductivity, G = 6 nS and 4.2 nS, respectively.

The fabrication of nanopores with controlled diameters is also interesting in the optimized detection of the translocation events of single objects. In fact, the dynamic range of a nanopore measures the detectable size range of analytes. Since the sensitivity is closely related to the relative size of the analyte and the nanopore, the limited dynamic range of a single nanopore has remained an issue, which means it is difficult to resolve two molecules that differ by a few nanometers in size. Moreover, while biomolecules such as DNA or proteins require nanopores with a diameter of a few nm, the detection of large NPs can be done only with larger nanopores. Here, we explored the electrical detection of dsDNA, and of AuNPs with sizes of 15 and 30 nm. This choice is aimed at the optimization of a platform that can be used in DNA nanostructures (comprising both DNA and nanomaterials) detection as in the case of DNA data storage, as illustrated in our recent review and in refs.[64–67]. The nanopore diameters used in

two sets of measurements were evaluated by their conductance, yielding ≈ 50 nm and 10 nm, used respectively for AuNPs and DNA detection. The results of these experiments are illustrated in Figure 4c,d. The DNA translocation data were first collected with a bandwidth of 200 kHz applying a constant voltage of 300 mV (see Figure S16, Note S13, Supporting Information). Following the approach recently reported by Xia et al.[68] we used a Bessel filter (low pass) to a cutoff of 20 kHz for event analysis (Figure 4c). The signal collected at 200 kHz showed rather high noise (≈ 1 nA peak to peak) and event detection was less noisy after filtering. This high and low-frequency noise level is comparable with similar results recently reported using the same electrical nanopore reader[68] and can be due to several parameters, such as surface conditions or contamination[69,70] and the nanotube geometry. After signal filtering, it was possible to clearly distinguish the events of translocation and to calculate the histogram for the entire ionic current versus time trace (Figure 4c). Here we can clearly distinguish two peaks: the baseline peak and a second peak corresponding to DNA events with a $\langle \Delta I \rangle DNA = 0.378 \pm 0.018$ nA. This single peak related to translocation events suggests that our system was not able to detect folded and unfolded DNA configurations. This could be due to the large pore diameter used in the experiment (≈10 nm), but also to the signal-to-noise ratio in our experiments.

In a second set of experiments, we used a nanopore prepared with a final diameter of ≈ 50 nm to detect events of translocation of mixed AuNPs (with diameters of 15 and 30 nm). The NPs were prepared according to the protocol reported in the Experimental Section and resulted as monodispersed NPs (see Note S14, Supporting Information). They were first characterized in terms of ζ-potential and resulted to be slightly negatively charged (≈ −25 mV). The translocation experiments were performed, with a bandwidth of 20 kHz, at different applied voltages observing zero or very few events of translocation for bias voltages below 500 mV. Translocation events, at a rate close to 10 events sec^{-1}, were detected with an applied voltage of 500 mV (Figure 4d). In this case, despite the low event rate, it was possible to observe two current levels ($\langle \Delta I \rangle AuNP_{15} = 0.22 \pm 0.03$ nA and $\langle \Delta I \rangle AuNP_{30} = 0.34 \pm 0.04$ nA) that can be associated to the two different NP sizes in the solution. The low event rate and the high voltage required to observe the translocation events can be ascribed to the low charge of the NPs and probably to the surface charges configuration in the nanotube/nanopore. As described in the Experimental Section, in order to avoid unpredictable surface charge configurations, the inner and outer parts of the nanotube/nanopore are coated with a 1 nm thick Al_2O_3 layer (with atomic layer deposition). This probably enabled to limit non-uniform charge distributions between the metal layer and the dielectric substrate/nanotube, but geometrical aspects (due for example to the high aspect ratio of the tube) can also play a role. For this reason, alternative geometries should be considered: for example, a conical shape for which it is reasonable to expect that the metallic nanopore can be prepared with the photocatalytic process with the same efficiency reported in this work.

To evaluate our nanopore platform for field-enhanced spectroscopies, as a final proof-of-concept experiment, we applied the nanopore arrays for SERS by recording the signal of ds-DNA (7 nM concentration) during the translocation through the pores. We used a setup similar to that reported in ref. [71], with laser excitation at 633 nm wavelength. For a direct comparison of the impact of the nanopore reduction, we compare the spectra obtained from nanopore arrays before and after the photocatalytic Au growth. We used Au deposition to be in resonance with the laser sources available in our Raman setup, since Au nanopores present a broad EM-field enhancement between 550 and 750 nm (see Figure S14, Note S11, Supporting Information). Au-Ag nanopores are more efficient in the spectral range between 350 and 450 nm as shown in Figure 4. Representative Raman spectra are reported in **Figure 5**, showing the two best signals obtained for the photochemically reduced pores and for the bare Au ring, respectively (details on the observed peaks are reported in Note S15, Supporting Information).[72] With the photochemical growth Au nanopore (black curve Figure 5a) it was possible to observe all the major peaks that can be associated to the ds-DNA vibration, with higher efficiency with respect to the bare Au ring (red curve). The time map reported in Figure 5a (right panel) shows the low event rate for this experiment. In fact, over 500 s of data collection, that is, 5000 spectra recorded (with an integration time of 100 msec), only a few tens of spectra showing translocation events were observed. This suggests a small dwell time as also observed in electrical recording. In any case, the ability of the plasmonic platform to enhance the detection of biomolecule translocation was confirmed. Finally, to corroborate the local field enhancement effect, we recorded spatial maps of the SERS intensity of an Au nanopore array covered with R6G as the target analyte, which are reported in Figure 5. Raman spectra of R6G molecules (concentration 0.1 mM) acquired from the array of 3D nanopores substrate exhibit all the major lines at 611, 773, 1127, 1183, 1310, 1360, 1507, 1573, and 1648 cm^{-1}. Each of the Raman spectra was corrected by subtracting the fluorescence background and the clear difference between spectra acquired from the nanopore area and the substrate demonstrates the enhancement due to the plasmonic field enhancement within the structure.[73]

3. Conclusion

In summary, we demonstrated that plasmonic photochemistry can be used to reduce the diameter of plasmonic nanopores down to 4 nm. With respect to previously reported plasmonic nanostructures, our approach ensures a controlled tuning of the nanopore diameter with nm-resolution. Another strength of our approach is that it can be applied to single nanopores, arrays of nanopores, or even arbitrary nanopore arrangements. The excellent control in nanopore size reduction over time (1 nm min^{-1} with Ag) enables the fabrication of single or multiple nanopores with controlled diameters that can be optimized for the detection of objects with different sizes. The fabrication of an array of nanopores with a wide range of sizes in a single platform could also be possible considering the slow rate of metal growth and the possibility to fabricate the initial metallic rings with different diameters playing with the FIB fabrication parameters, in particular the ion current. It would be not difficult to prepare initial rings with different sizes (as discussed above initial diameters between 50 and 1000 nm are possible to fabricate) and then shrink them down to different pore diameters in a single chip. Nanopores with sub-10 nm apertures lead to very strong EM field enhancement, which makes this platform

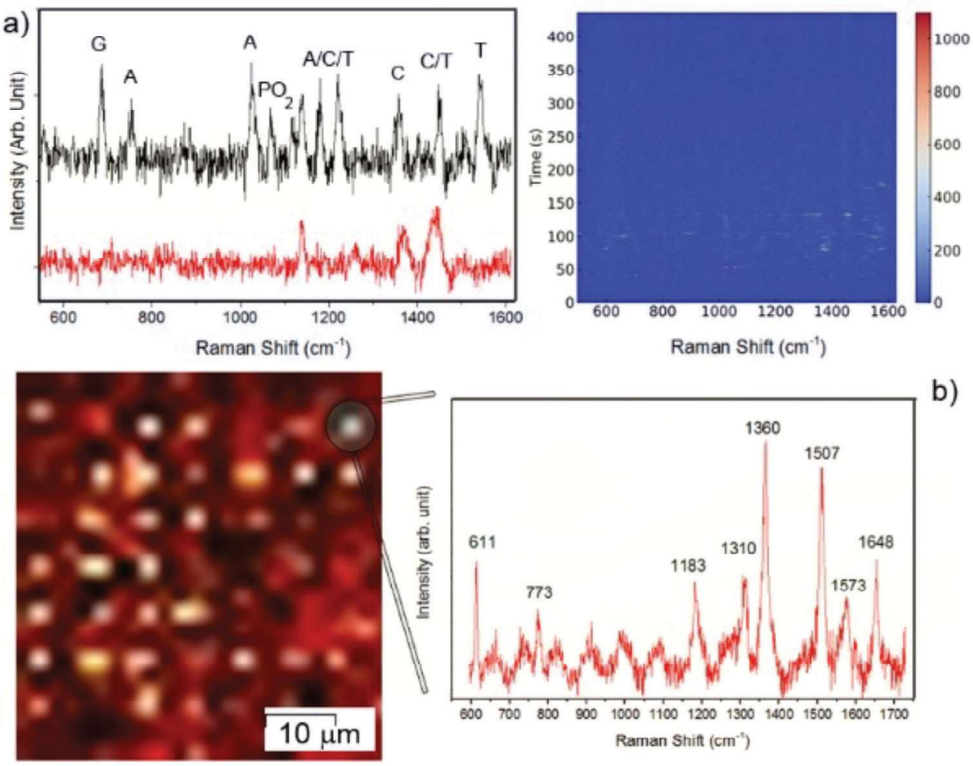

Figure 5. a) SERS spectra of dsDNA translocating through an Au ring on top of the pillar (black curve) and an Au nanopore (red curve) and time trace over 500 s, integration time 0.1 sec; b) map of the Raman spectra obtained from 3D nanopores array with R6G as analyte. The bright spots represent the nanopore, where the intensity of the acquired spectra was significantly higher with respect to the substrate. The map is obtained by integrating the signal at 1360 cm^{-1}; this peak is selected because it resulted to be the most frequently detected in the whole dataset. A detail on the full spectrum obtained from a single nanopore is also reported.

appealing for field-enhanced spectroscopies such as fluorescence, FRET and SERS.[8] As a proof-of-concept, we demonstrate that our nanopores can detect very small objects such as dsDNA and also larger objects as metallic nanoparticles with a diameter of a few tens of nm. Furthermore, we think that the plasmonic photochemistry approach that we presented is not limited to the metallic ring geometry or even nanopores, but it can be applied in general to any kind of plasmonic structures with a well-defined spatial EM-field enhancement. Also, we believe that such a flexible approach represents a valuable tool to investigate plasmon-driven photochemical reactions, charge transfer and other intriguing nanoscale chemical phenomena, even at ultrafast timescales. Finally, this method might be an important step toward the realization of new plasmonic devices for several applications, from nanopore-based single-molecule detection[37] and DNA or protein sequencing to ion selectivity[74] and light-based multiplexing information processing.[64,75]

4. Experimental Section

Fabrication Procedures: Freestanding Si_3N_4 membrane chips were prepared following a standard membrane fabrication procedure. In particular, an array of square membranes was prepared on a commercial double-sided 100 nm LPCVD Si_3N_4 coated 500 µm Si wafer via UV photolithography, following reactive ion etching and subsequent KOH wet etching.

Hollow nanopillars were fabricated by using a reported procedure.[47] In brief, properly diluted S1813 MICROPOSIT photoresist was spin-coated onto the Si_3N_4 chips. Then a thin layer (80 nm) of Au was deposited via sputtering. FIB patterning was used to expose the resist in arbitrary arrays by using different ion currents (24, 40, 80 and 230 pA, respectively). The choice of different ion currents allowed for the preparation of different diameters in the final pillar/Au ring. After the exposure, the Au top layer was removed with a gold etchant (KI solution), followed by oxygen plasma treatment (100 W 180 s) to clean the upper part of the resist layer. A development in acetone with a further oxygen plasma (100 W 150 s) produced the final hollow dielectric structure. A thin layer of Ti//Au (2//30 nm) was then deposited on top of nanopillars via electron beam evaporation. The photochemical reaction was obtained by immersing the substrate in a silver nitrate solution that was prepared with 30 mL 10 mM $AgNO_3$/ 1.8 mL and 6 mM Sodium citrate and then illuminated with white light (Xe lamp 50 W / 20 × 0.95 NA objective) using an optical microscope equipped with a 20× objective. For gold deposition, 5.0, 0.5 and 0.05 mM $AuBr_3$, and 10 mM $HAuCl_4$ solutions were used. After the exposures, the samples were rinsed in isopropyl alcohol and dried under N_2 flow.

To note, similar fabrication procedures could be applied replacing the 30 nm thick Au rings with similar rings prepared with an Ag coating obtaining comparable enhancement in the visible range (see Note S16, Supporting Information).

Planar pores were fabricated with FIB on Si_3N_4 membranes previously coated with a thin layer of Ti//Au (2//50 nm). The substrate was immersed in a Silver nitrate solution that was prepared with 30 mL 10 mM $AgNO_3$/ 1.8 mL 6 mM Sodium citrate and then illuminated with 638 nm laser light for different durations.[40] After the exposures, the samples were rinsed in isopropyl alcohol and dried under N2 flow.

Electrical Characterization: Electrical measurements were conducted in 10 mM Tris-HCl/ 1 mM EDTA buffer solution, in the dark or under illumination with a LED at 650 nm, and 460 nm (power 2 mW) inside a nanopore reader using Ag/AgCl electrodes.[55]

Electrical readout of DNA and NPs translocations were conducted in 1 M KCl by using the same instrument/reader from Elements srl.[68]

Raman Spectroscopy: Raman spectroscopy measurements were performed using a Renishaw InVia Raman system with a 100 × 0.95 NA water immersion objective. The signal from a dsDNA was collected for 500 s through the pore with an integration time of 0.1 s. In this case, an excitation wavelength of 632.8 nm was used for the experiment performed with an Au ring and Au-reduced nanopores. The dsDNA was 7 nM λ-DNA dispersed in 1 M KCl. In order to enable the translocation, the solution was dropped in the bottom side of the membrane, while the upper side was filled with the buffer alone and moved close to the microscope objective used to excite the sample and collect the spectrum, a voltage of 100 mV was applied. A second experiment was performed by using R6G (0.1 mM) dispersed in H_2O without externally applied voltage. The use of a resonant Raman molecule, excited at 632 nm, was chosen in order to rapidly test the in-array spectroscopy.

Dynamic Light Scattering: Dynamic light scattering experiments were performed by using a Malvern Zetasizer, and the measurements were analyzed with Zetasizer software. Data were reported as the average of three measurements. The procedure used for these measurements followed the protocol reported in ref. [76].

Numerical Simulations: Numerical simulations were carried out using the finite element method implemented in the RF solver of the commercial COMSOL Multiphysics software. The geometry was set up in 3D, and perfectly matched layers were introduced to suppress back reflections from domain walls. Linearly polarized light (plane wave) at different wavelengths was injected at the top of the simulation geometry under normal incidence to the structures. Interpolated data from Rakić et al.[77] was used to describe the linear optical properties of silver and gold. The refractive index of the dielectric pillars and the environment were set to 1.45 and 1.33, respectively.

Synthesis of 15 and 30 nm PEGylated Au NPs: Chemicals: Sodium borohydride (ReagentPlus, ≥99%, NaBH4), poly(ethylene glycol) methyl ether thiol average Mn 2000 and 6000, *L*-ascorbic acid (ACS reagents, ≥99%, AA), hypochlorite (6–14% active chlorine), and cetyltrimethylammonium chloride (≥98%, CTAC) were purchased from Sigma Aldrich. HAuCl4·3 H2O (≥99.9%, trace metal basis) was purchased from Alfa Aesar. All solutions, except HAuCl4 and CTAB, were prepared immediately before use. Purified Milli-Q water was used in all experiments (Millipore, 18.2 MΩ cm). Glassware was cleaned with aqua regia and rinsed extensively with Milli-Q water before use.

Synthesis and Functionalization of Au NPs: Gold nanospheres, Au15 and Au30, were synthesized according to the Turkevich[78] and seeded[79] methods, respectively. For ligand exchange, the particles were mixed with thiolated PEG ligands in water (PEG2K for the case of Au15 and PEG6k for Au30 NPs), to obtain a final Au0 concentration of 1 mM (according to the absorbance at 400 nm) and a PEG-SH content of 1 mg mL^{-1}. After stirring overnight at room temperature, the excess of PEG-SH was removed by centrifugation at 12 000 rpm (Au15) or 4800 rpm (Au30) and the pellets were redispersed in water.

Electron Microscopy Characterization: AuNPs were characterized by means of TEM. TEM images were obtained using a JEOL microscope at an acceleration voltage of 200 kV. Approximately 3 µL of the sample was dropped on a lacey carbon-coated grid and left to dry. The size distribution of the nanoparticles obtained was analyzed using ImageJ software. The nanopores were characterized by using an SEM FEI Nova 600i equipped with EDS.

Supporting Information

Supporting Information is available from the Wiley Online Library or from the author.

Acknowledgements

D.G. and R.K. acknowledge funding from the European Union under the H2020 Programme (No. FETOPEN-01-2018-2019-2020, Grant No. 964995 "DNAFAIRYLIGHTS"). N.M. acknowledges support from the European Union under the H2020 Programme (FETOPEN-01-2018-2019-2020 Grant No. 964363 "ProID"), the European Union under the Horizon Europe Programme (HORIZON-EIC-2021-PATHFINDEROPEN-01-01 Grant No. 101046920 "iSenseDNA"), the Swedish Research Council (Grant No. 2021–05784), and the Kempestiftelserna (Grant No. JCK-3122). T. W. acknowledges support from the Swedish Research Council (Grant n. 202-104629). The authors thank E. Miele for the support in SERS data analysis, M. Dipalo for the help with the TOC figure, and M. Ardini and G. Giovannini for the support on preliminary tests and fruitful discussions on photochemistry depositions. The Authors acknowledge the support from the Nanofabrication Facility at Istituto Italiano di Tecnologia.

Conflict of Interest

The authors declare no conflict of interest.

Author Contributions

G.L. and J.K. contributed equally to this work. D.G. and N.M. conceived the idea and coordinated the experimental and theoretical activities, respectively; G.L. fabricated and characterized the structures; J.K. and L.L. performed the numerical simulations; A.D. and A.D. performed the electrical measurements; K.R.K. and I.G. synthetized the Au NPs; A.V.R., T.W., and R.K. contributed to the scientific discussion and data interpretation.

Data Availability Statement

The data that support the findings of this study are available from the corresponding authors upon request.

Keywords

enhanced spectroscopy, nanopores, photocatalytic process, plasmonics, single-molecule detection

Received: April 2, 2023
Revised: April 20, 2023
Published online:

[1] Z. Liu, Y. Wang, T. Deng, Q. Chen, *J. Nanomater.* **2016**, *2016*, 5284786.
[2] R. Hu, X. Tong, Q. Zhao, *Adv. Healthcare Mater.* **2020**, *9*, 2000933.
[3] B. N. Miles, A. P. Ivanov, K. A. Wilson, F. Doğan, D. Japrung, J. B. Edel, *Chem. Soc. Rev.* **2013**, *42*, 15.
[4] F. Sawafta, B. Clancy, A. T. Carlsen, M. Huber, A. R. Hall, *Nanoscale* **2014**, *6*, 6991.
[5] H. Zhang, X. Duan, Z. Tang, D. Zhang, W. Pang, W. F. Cui, *Nanomater. Nanotechnol.* **2016**, *6*, 35.
[6] M. Waugh, K. Briggs, D. Gunn, M. Gibeault, S. King, Q. Ingram, A. M. Jimenez, S. Berryman, D. Lomovtsev, L. Andrzejewski, V. Tabard-Cossa, *Nat. Protoc.* **2020**, *15*, 122.
[7] W. Lu, R. Hu, X. Tong, D. Yu, Q. Zhao, *Small Struct.* **2020**, *1*, 2000003.
[8] W. Li, J. Zhou, N. Maccaferri, R. Krahne, K. Wang, D. Garoli, *Anal. Chem.* **2022**, *94*, 503.
[9] D. V. Verschueren, S. Pud, X. Shi, L. D. Angelis, L. Kuipers, C. Dekker, *ACS Nano* **2019**, *13*, 61.
[10] T. Gilboa, C. Torfstein, M. Juhasz, A. Grunwald, Y. Ebenstein, E. Weinhold, A. Meller, *ACS Nano* **2016**, *10*, 8861.

[11] O. N. Assad, N. D. Fiori, A. H. Squires, A. Meller, *Nano Lett.* **2015**, *15*, 745.
[12] H. Im, N. J. Wittenberg, A. Lesuffleur, N. C. Lindquist, S. H. Oh, *Chem. Sci.* **2010**, *1*, 688.
[13] M. P. Cecchini, A. Wiener, V. A. Turek, H. Chon, S. Lee, A. P. Ivanov, D. W. McComb, J. Choo, T. Albrecht, S. A. Maier, J. B. Edel, *Nano Lett.* **2013**, *13*, 4602.
[14] M. P. Jonsson, C. Dekker, *Nano Lett.* **2013**, *13*, 1029.
[15] S. Nam, I. Choi, C. C. Fu, K. Kim, S. Hong, Y. Choi, A. Zettl, L. P. Lee, *Nano Lett.* **2014**, *14*, 5584.
[16] S. A. Maier, B. Ng, M. P. Cecchini, C. R. Crick, J. B. Edel, P. Albella, T. Roschuk, A. P. Ivanov, F. Bresme, *Nano Lett.* **2014**, *15*, 553.
[17] F. Nicoli, D. Verschueren, M. Klein, C. Dekker, M. P. Jonsson, *Nano Lett.* **2014**, *14*, 6917.
[18] C. Plesa, D. Verschueren, S. Pud, N. Vukovic, C. Dekker, M. P. Jonsson, *Nano Lett.* **2015**, *15*, 7112.
[19] L. Deng, Y. Wang, C. Liu, D. J. J. Hu, P. P. Shum, L. Su, *Opt. Commun.* **2016**, *372*, 113.
[20] C. Chen, Y. Li, S. Kerman, P. Neutens, K. Willems, S. Cornelissen, L. Lagae, T. Stakenborg, P. V. Dorpe, *Nat. Commun.* **2018**, *9*, 1733.
[21] D. Garoli, D. Mosconi, E. Miele, N. Maccaferri, M. Ardini, G. Giovannini, M. Dipalo, S. Agnoli, F. D. Angelis, *Nanoscale* **2018**, *10*, 17105.
[22] D. Verschueren, X. Shi, C. Dekker, *Small Methods* **2019**, *3*, 1800465.
[23] G. Giovannini, M. Ardini, N. Maccaferri, X. Zambrana-Puyalto, G. Panella, F. Angelucci, R. Ippoliti, D. Garoli, F. D. Angelis, *Adv. Opt. Mater.* **2020**, *8*, 1901583.
[24] X. Zambrana-Puyalto, P. Ponzellini, N. MacCaferri, D. Garoli, *Phys. Rev. Appl.* **2020**, *14*, 054065.
[25] Q. Shen, P. L. Zhou, B. T. Huang, J. Zhou, H. L. Liu, S. A. Ahmed, X. L. Ding, J. Li, Y. M. Zhai, K. Wang, *J. Electroanal. Chem.* **2021**, *894*, 115373.
[26] H. L. Liu, J. Cao, S. Hanif, C. Yuan, J. Pang, R. Levicky, X. H. Xia, K. Wang, *Anal. Chem.* **2017**, *89*, 10407.
[27] J. Cao, H.-L. Liu, J.-M. Yang, Z.-Q. Li, D.-R. Yang, L.-N. Ji, K. Wang, X.-H. Xia, *ACS Sens.* **2020**, *5*, 2198.
[28] J. Zhou, P.-L. Zhou, Q. Shen, S. A. Ahmed, X.-T. Pan, H.-L. Liu, X.-L. Ding, J. Li, K. Wang, X.-H. Xia, *Anal. Chem.* **2021**, *93*, 11679.
[29] O. N. Assad, T. Gilboa, J. Spitzberg, M. Juhasz, E. Weinhold, A. Meller, *Adv. Mater.* **2017**, *29*, 1605442.
[30] Y. Goto, I. Yanagi, K. Matsui, T. Yokoi, K. I. Takeda, *Sci. Rep.* **2016**, *6*, 31324.
[31] H. Kwok, K. Briggs, V. Tabard-Cossa, *PLoS One* **2014**, *9*, e92880.
[32] A. T. Carlsen, K. Briggs, A. R. Hall, V. Tabard-Cossa, *Nanotechnology* **2017**, *28*, 085304.
[33] E. Zvuloni, A. Zrehen, T. Gilboa, A. Meller, *ACS Nano* **2021**, *15*, 12189.
[34] Z. Tang, M. Dong, X. He, W. Guan, *ACS Appl. Mater. Interfaces* **2021**, *13*, 13383.
[35] J. P. Fried, J. L. Swett, B. P. Nadappuram, J. A. Mol, J. B. Edel, A. P. Ivanov, J. R. Yates, *Chem. Soc. Rev.* **2021**, *50*, 4974.
[36] J. D. Spitzberg, A. Zrehen, X. F. v. Kooten, A. Meller, *Adv. Mater.* **2019**, *31*, 1900422.
[37] D. Garoli, H. Yamazaki, N. MacCaferri, M. Wanunu, *Nano Lett.* **2019**, *19*, 7553.
[38] G. Baffou, R. N. f. C. Quidant, *Chem. Soc. Rev.* **2014**, *43*, 3898.
[39] E. Cortés, R. Grzeschik, S. A. Maier, S. Schlücker, *Nat Rev Chem* **2022**, *6*, 259.
[40] B. Ai, Z. Wang, H. Möhwald, G. Zhang, *ACS Nano* **2017**, *11*, 12094.
[41] P. Gu, W. Zhang, G. Zhang, *Adv. Mater. Interfaces* **2018**, *5*, 1800648.
[42] Z. Wang, B. Ai, H. Möhwald, G. Zhang, *Adv. Opt. Mater.* **2018**, *6*, 1800402.
[43] Y. Guan, Z. Wang, P. Gu, Y. Wang, W. Zhang, G. Zhang, *Nanoscale* **2019**, *11*, 9422.
[44] L. Zhang, P. Chen, A. Loiseau, D. Brouri, S. Casale, M. Salmain, S. Boujday, B. Liedberg, *J. Phys. Chem. C* **2019**, *123*, 10614.
[45] A. Zhu, R. Gao, X. Zhao, F. Zhang, X. Zhang, J. Yang, Y. Zhang, L. Chen, Y. Wang, *Nanoscale* **2019**, *11*, 6576.
[46] Z. Wang, B. Ai, Y. Guan, Y. Wang, G. Zhang, *Sens. Actuators, B* **2021**, *329*, 129220.
[47] X. Zambrana-Puyalto, N. Maccaferri, P. Ponzellini, G. Giovannini, F. D. Angelis, D. Garoli, *Nanoscale Adv* **2019**, *1*, 2454.
[48] F. De Angelis, M. Malerba, M. Patrini, E. Miele, G. Das, A. Toma, R. P. Zaccaria, E. Di Fabrizio, *Nano Lett.* **2013**, *13*, 3553.
[49] G. C. Messina, X. Zambrana-Puyalto, N. Maccaferri, D. Garoli, F. D. Angelis, *Nanoscale* **2020**, *12*, 8574.
[50] D. Garoli, E. Calandrini, A. Bozzola, M. Ortolani, S. Cattarin, S. Barison, A. Toma, F. D. Angelis, *Nanoscale* **2017**, *9*, 915.
[51] C. Turro, W. J. Dressick, *ACS Appl. Electron. Mater.* **2022**, *4*, 5664.
[52] A. Rutkowska, K. Freedman, J. Skalkowska, M. J. Kim, J. B. Edel, T. Albrecht, *Anal. Chem.* **2015**, *87*, 2337.
[53] M. Ayub, A. Ivanov, J. Hong, P. Kuhn, E. Instuli, J. B. Edel, T. Albrecht, *J. Phys.: Condens. Matter* **2010**, *22*, 454128.
[54] N. H. Pham, Y. Yao, C. Wen, S. Li, S. Zeng, T. Nyberg, T. T. Tran, D. Primetzhofer, Z. Zhang, S.-L. Zhang, *ACS Nano* **2021**, *15*, 17938.
[55] D. J. Niedzwiecki, Y.-C. Chou, Z. Xia, F. Thei, M. Drndić, *Rev. Sci. Instrum.* **2020**, *91*, 031301.
[56] H. Yang, M. Saqib, R. Hao, *Front. Chem.* **2021**, *9*, 664820.
[57] R. Wu, Y. Wang, Z. Zhu, C. Yu, H. Li, B. Li, S. Dong, *ACS Appl. Mater. Interfaces* **2021**, *13*, 9482.
[58] Y. He, M. Tsutsui, Y. Zhou, X. S. Miao, *NPG Asia Mater.* **2021**, *13*, 48.
[59] B. A. Shepherd, M. R. E. Tanjil, Y. Jeong, B. BaloÄaylu, J. Liao, M. C. Wang, *MRS Adv.* **2020**, *5*, 2889.
[60] Y. Luo, L. Wu, J. Tu, Z. Lu, *Int. J. Mol. Sci.* **2020**, *21*, 2808.
[61] Q. Chen, Z. Liu, *Sensors* **2019**, *19*, 1886.
[62] C. R. Crick, P. Albella, B. Ng, A. P. Ivanov, T. Roschuk, M. P. Cecchini, F. Bresme, S. A. Maier, J. B. Edel, *Nano Lett.* **2015**, *15*, 553.
[63] G. Groeseneken, K. Willems, T. Stakenborg, Y. Li, L. Lagae, C. Chen, P. V. Dorpe, *Nanoscale* **2016**, *8*, 12324.
[64] A. Doricchi, C. M. Platnich, A. Gimpel, F. Horn, M. Earle, G. Lanzavecchia, A. L. Cortajarena, L. M. Liz-Marzán, N. Liu, R. Heckel, R. N. Grass, R. Krahne, U. F. Keyser, D. Garoli, *ACS Nano* **2022**, *16*, 17552.
[65] J. Zhu, N. Ermann, K. Chen, U. F. Keyser, *Small* **2021**, *17*, 2100711.
[66] F. Bošković, A. Ohmann, U. F. Keyser, K. Chen, *Small Struct.* **2021**, *2*, 2000144.
[67] K. Chen, J. Zhu, F. Bošković, U. F. Keyser, *Nano Lett.* **2020**, *20*, 3754.
[68] Z. Xia, A. Scott, R. Keneipp, J. Chen, D. J. Niedzwiecki, B. DiPaolo, M. Drndić, *ACS Nano* **2022**, *16*, 18648.
[69] A. Fragasso, S. Schmid, C. Dekker, *ACS Nano* **2020**, *14*, 1338.
[70] R. M. M. Smeets, U. F. Keyser, N. H. Dekker, C. Dekker, *Proc. Natl. Acad. Sci. U. S. A.* **2008**, *105*, 417.
[71] A. Hubarevich, J.-A. Huang, G. Giovannini, A. Schirato, Y. Zhao, N. Maccaferri, F. D. Angelis, A. Alabastri, D. Garoli, *J. Phys. Chem. C* **2020**, *124*, 22663.
[72] C. Otto, T. J. J. v. d. Tweel, F. F. M. d. Mul, J. Greve, *J. Raman Spectrosc.* **1986**, *17*, 289.
[73] P. Hildebrandt, M. Stockburger, *J. Phys. Chem.* **1984**, *88*, 5935.
[74] H. Zhang, X. Li, J. Hou, L. Jiang, H. Wang, *Chem. Soc. Rev.* **2022**, *51*, 2224.
[75] F. Bošković, U. F. Keyser, *Nat. Chem.* **2022**, *14*, 1258.
[76] J. Huang, M. Z. Mousavi, Y. Zhao, A. Hubarevich, F. Omeis, G. Giovannini, M. Schütte, D. Garoli, F. D. S. Angelis, *Nat. Commun.* **2019**, *10*, 5321.
[77] A. D. Rakic, A. B. Djurisic, J. M. Elazar, M. L. Majewski, *Appl. Opt.* **1998**, *37*, 5271.
[78] J. Turkevich, P. C. Stevenson, J. Hillier, *Discuss. Faraday Soc.* **1951**, *11*, 55.
[79] C. Hanske, G. González-Rubio, C. Hamon, P. Formentín, E. Modin, A. Chuvilin, A. Guerrero-Martínez, L. F. Marsal, L. M. Liz-Marzán, *J. Phys. Chem. C* **2017**, *121*, 10899.